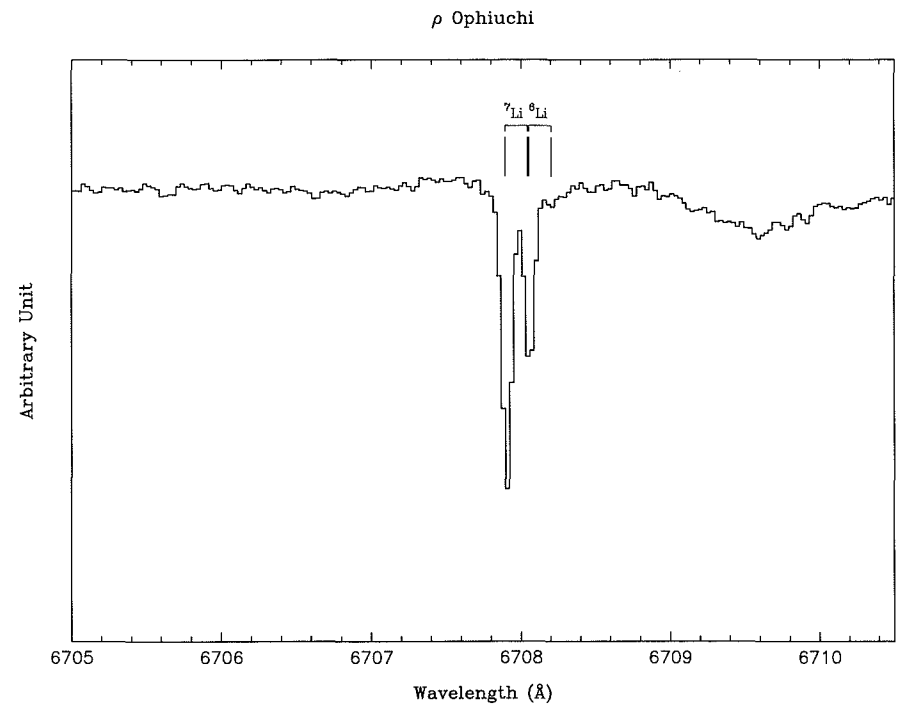


detection of the weaker ${}^6\text{Li}$ component.

Further speculations on this spectrum are still premature. Only a detailed analysis with the profile fitting method developed by Vidal-Madjar et al. (1977) and Ferlet et al. (1980 a, b) may help to evaluate with precision the interstellar lithium isotopic ratio. This method was already applied to the interstellar Li lines towards ζ Oph by Ferlet and Dennefeld (1984), yielding the above-mentioned result. It offers the possibility of extracting all the information contained in the profile, particularly the velocity structure along the line of sight (previous articles indicate the presence of two components), and allows calculation of the blend between the isotopes lines. This will be the scope of a forthcoming paper on the present data.

While the study of the interstellar lithium isotopic ratio is of crucial importance for nucleosynthesis and chemical evolution, it is certainly not an easy task. The observation of extremely weak interstellar lithium lines towards relatively faint star requires a very efficient instrumentation. The 3.6-m + CES via fiber link fulfils this quite well, as can be judged by the quality of the present data, provided great care is taken during the observations and data reduction.

Moreover, observations in July 1991 with the CAT revealed new good candidates for the interstellar lithium ratio, especially σ Sco, and χ Oph, which were observed for the first time at this wavelength. Their total Li equivalent width have not been precisely estimated yet, but we hope to investigate these new lines of sight. We will also continue to accumulate photons from ρ Oph to further improve the S/N in order to definitely detect the weakest ${}^6\text{Li}$ line. Still, the perspective of the VLT brings new hope for this difficult task; it should even



allow measurements of the abundance of lithium in the Magellanic Clouds.

Acknowledgements

We would like to express our thanks to the ESO staff at La Silla, especially to the Operation Group, and to Philippe Bertin for his help during the data reduction.

References

Avila, G., D'Odorico, S.: 1988, Proceedings of the ESO Conference on Very Large Telescopes and their Instrumentation, Garching, 21-24 March 1988, p. 1121.
Dearborn, D., Schramm, D., Steigman, G., Truran, J.: 1989, *Astrophys. J.*, **347**, 455.

Ferlet, R., Laurent, C., Vidal-Madjar, A., York, D.G.: 1980a, *Astrophys. J.*, **235**, 478.
Ferlet, R., Vidal-Madjar, A., Laurent, C., York, D.G.: 1980b, *Astrophys. J.*, **242**, 576.
Ferlet, R., Dennefeld, M.: 1984, *Astron. Astrophys.*, **138**, 203.
Kawano, A.: 1988, *Astrophys. J. Letters*, **327**, L750.
Hobbs, L.M.: 1975, *Astrophys. J.*, **200**, 621.
Hobbs, L.M., Pilachowski, C.: 1988, *Astrophys. J.*, **334**, 750.
Reeves, H.: 1988, *European Journal of Physics*, **9**, 179.
Scalo, J.M.: 1976, *Astrophys. J.*, **206**, 795.
Spite, F., Spite, M.: 1982, *Astron. Astrophys.*, **115**, 357.
Starrfield, S., Truran, J.W., Sparks, W.M., Arnould, M.: 1978, *Astrophys. J.*, **222**, 600.
Vangioni-Flam, E., Casse, M., Oberto, Y.: 1989, *Astrophys. J.*, **349**, 510.
Vidal-Madjar, A., Laurent, C., Bonnet, R.M., York, D.G.: 1977, *Astrophys. J.*, **211**, 91.

On Flux Calibration of Spectra

M.A. FLUKS and P.S. THÉ, *Astronomical Institute, University of Amsterdam, the Netherlands*

1. Introduction

In an A&A paper on spectroscopic reduction, two spectral correction functions for the spectral range $375 < \lambda[\text{nm}] < 900$ were derived (Fluks and Thé, 1992). The first $\chi_e(\lambda)$, accounts for the depletion of stellar radiation in the Earth's atmosphere and the second, $\chi_s(\lambda)$, for the blocking of part of the radiation by the spectrograph slit. In the present paper we summarize the main results for those observers who are in-

terested in our method but not in the mathematical part of the problem.

The atmospheric scattering and molecular absorption at ESO is given in Table 1, and using Table 3, one can correct for the blocking of part of the radiation by the spectrograph slit. We derived formulas for two slit positions: in the west-east direction in the horizontal plane and in the hour angle declination in the elevated plane. By applying our method, the spectral flux-calibration will be more accurate.

In the three (artificial) wavelength-calibrated spectra, shown in Figure 1, $f_1(\lambda)$ is the spectrum before entering the atmosphere ($= F(\lambda)\chi_{\text{resp}}(\lambda)$, in which $F(\lambda)$ is the flux-calibrated spectrum and $\chi_{\text{resp}}(\lambda)$ is the instrumental response function), $f_2(\lambda)$ is the spectrum after its passage through the atmosphere and $f_3(\lambda)$ is the "observed" CCD spectrum.

$\chi_e(\lambda) = \chi_{\text{sc}}(\lambda)\chi_a(\lambda)$ is the spectral transparency function of the atmosphere in which $\chi_{\text{sc}}(\lambda)$ accounts for the scattering (Aerosol scattering and Rayleigh scat-

Table 1 A: The continuous spectral scattering and absorption of the Earth's atmosphere at ESO at $z = 0^\circ$.

λ [nm]	$a_e(\lambda)$ [mag]	$a_a(\lambda)$ [mag]	λ [nm]	$a_e(\lambda)$ [mag]	$a_a(\lambda)$ [mag]	λ [nm]	$a_e(\lambda)$ [mag]	$a_a(\lambda)$ [mag]
375.0	0.3849	0.0000	720.0	0.0403	0.0758	764.0	0.0348	0.3495
400.0	0.2900	0.0000	730.0	0.0388	0.0753	765.0	0.0345	0.2610
450.0	0.1805	0.0000	740.0	0.0373	0.0163	767.5	0.0342	0.1245
475.0	0.1517	0.0020	750.0	0.0365	0.0000	770.0	0.0340	0.0557
500.0	0.1324	0.0065	757.0	0.0356	0.0017	772.5	0.0335	0.0219
525.0	0.1155	0.0120	757.5	0.0355	0.0035	774.0	0.0333	0.0054
550.0	0.1010	0.0207	758.0	0.0355	0.0071	775.0	0.0332	0.0000
580.0	0.0859	0.0269	758.5	0.0355	0.0167	780.0	0.0325	0.0000
600.0	0.0762	0.0178	759.0	0.0354	0.0478	799.0	0.0298	0.0013
625.0	0.0650	0.0112	759.2	0.0354	0.1370	800.0	0.0297	0.0038
650.0	0.0548	0.0066	759.5	0.0353	0.4101	801.0	0.0295	0.0067
675.0	0.0476	0.0026	760.0	0.0353	0.7422	802.0	0.0294	0.0098
685.0	0.0456	0.0093	760.2	0.0352	0.8410	805.0	0.0289	0.0205
686.0	0.0455	0.0317	760.5	0.0352	0.8983	810.0	0.0280	0.0519
687.0	0.0453	0.2198	760.6	0.0351	0.8749	815.0	0.0272	0.1181
687.1	0.0453	0.2173	760.8	0.0351	0.8039	820.0	0.0264	0.2350
687.5	0.0452	0.1648	761.0	0.0351	0.7283	821.0	0.0262	0.2484
688.0	0.0451	0.0614	761.4	0.0350	0.4327	821.5	0.0261	0.2504
688.2	0.0451	0.0202	761.8	0.0350	0.1994	822.0	0.0260	0.2484
688.5	0.0450	0.0737	761.9	0.0350	0.1923	825.0	0.0255	0.1818
689.0	0.0450	0.0986	762.0	0.0350	0.2212	830.0	0.0246	0.0850
690.0	0.0448	0.0715	762.4	0.0349	0.4539	835.0	0.0238	0.0370
691.0	0.0446	0.0553	762.6	0.0349	0.4939	840.0	0.0229	0.0128
695.0	0.0440	0.0225	762.8	0.0349	0.4800	850.0	0.0212	0.0000
700.0	0.0432	0.0176	763.0	0.0349	0.4621	875.0	0.0170	0.0000
710.0	0.0417	0.0334	763.5	0.0348	0.4060	900.0	0.0127	0.0000

Table 1 B: The characteristics of the absorption bands (Kondratyev 1969).

Denomination of band	Absorbing molecule	Spectral region [nm]	Band centre position [nm]
Chappuis	O ₃	440 – 750	580
B	O ₂	685 – 702	687
α	H ₂ O	700 – 740	718
A	O ₂	758 – 775	760
0.8 μ m	H ₂ O	800 – 843	821

tering) and $\chi_a(\lambda)$ for the molecular absorption bands (H₂O, O₂ and O₃).

If in the spectroscopic reduction the observed spectra of standard stars are not corrected for $\chi_e(\lambda)\chi_s(\lambda)$, the instrumental response function $\chi_{resp}(\lambda)$ deduced from these spectra will be biased by this factor. In this paper, the spectral functions $\chi_e(\lambda)$ and $\chi_s(\lambda)$ are removed from the instrumental response function $\chi_{resp}(\lambda)$ so that the $\chi_{resp}(\lambda)$, deduced from the observations of standard stars, becomes independent of the position of these stars.

2. The Spectral Transparency of the Earth's Atmosphere

Due to continuous atmospheric scattering and atmospheric molecular absorption, atmospheric features are superimposed onto those in stellar spectra. By normalizing the spectra of white dwarfs, having few or no intrinsic spectral features in the spectral regions of Table 1, the absorbing component $\chi_a(\lambda)$ of $\chi_e(\lambda)$ can be found. The slowly

varying continuous functions $\chi_{sc}(\lambda)$ and $\chi_s(\lambda)$ resolve in the normalizing procedure, so that $\chi_a(\lambda)$ can be obtained from the observation: $\chi_a(\lambda) = \frac{f_3(\lambda)}{f_4(\lambda)}$ in which $f_4(\lambda)$ is the normalized spectrum of $f_3(\lambda)$

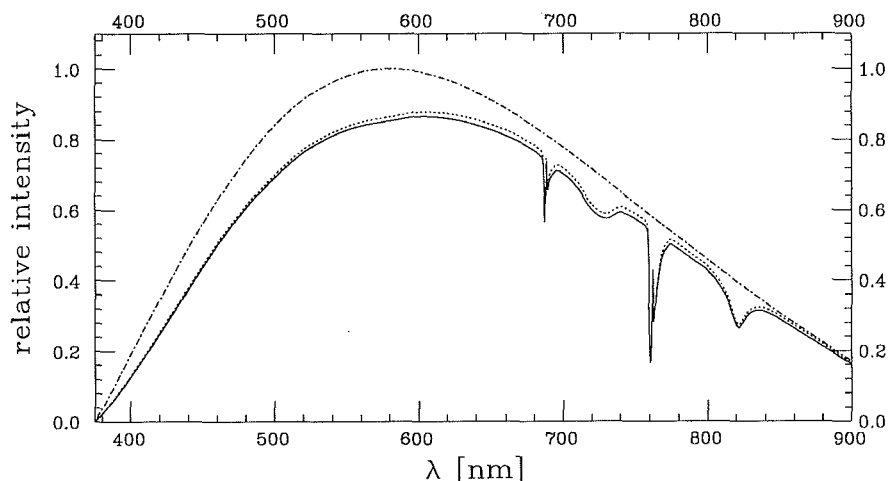


Figure 1: Three wavelength-calibrated spectra: $f_1(\lambda)$ (dot-dashed curve), $f_2(\lambda)$ (dotted curve) and $f_3(\lambda)$ (solid curve) for a star at $z = A = 45^\circ$ with surface brightness dispersion $\sigma = 0''.800$ and a horizontal mounted spectrograph slit of sizes $2a \times 2b = 5'' \times 240''$.

(see Fig. 2). Tüg (1977) gives the summation of the Aerosol scattering, the Rayleigh scattering and the absorption by ozone in magnitudes $a_a(\lambda)$ at zenith distance $z=0^\circ$ at ESO. Removing the ozone component from Tügs $a_e(\lambda)$ at $z=45^\circ$, the corresponding continuous scattering component of the spectral transparency function, $\chi_{sc}(\lambda)$ is found. Next, $\chi_e(\lambda)$ at $z=45^\circ$ and at $z=0^\circ$ are obtained. These results are displayed in Figure 2 and Figure 3, respectively. Table 1A gives the spectral scattering and absorption of the Earth's atmosphere at ESO at $z=0^\circ$, and Table 1B the denomination of the absorbing bands, the spectral region, and the band centre positions (Kondratyev, 1969). Note that the entries in Table 1A are still subject to nocturnal and annual variations (especially of H₂O). Other workers in spectroscopy might adjust the results of Table 1A to their own observational conditions.

Two sharply double-peaked oxygen absorption bands are encountered, centred at 687 and 760 nm, respectively. The two water vapour absorption bands centred at 718 and 821 nm are too weak and there is too much scatter in the normalized spectra to reveal the real structure inside these bands (there are subfeatures at 816.4, 817.7 and 822.7 nm). By replacing the MIDAS table ATMEOEXAN, containing Tügs $a_e(\lambda)$, by NEWATMEOEXAN, containing the $a_e(\lambda)$, obtained from Table 1A, stellar spectra can be corrected for atmospheric scattering plus absorption, at a specific airmass, using MIDAS routine EXTINCTION/SPECTRUM.

3. The Spectral Transmittance at the Spectrograph Slit

Light of either end of a stellar spectrum will be more lost compared to that at the centre, since the slit has finite

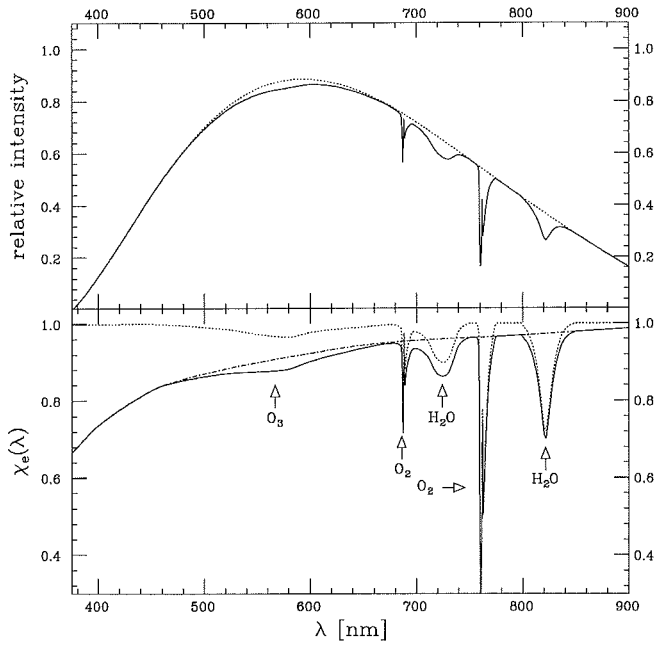


Figure 2: The top frame shows the normalizing procedure. The solid curve is the "observed" spectrum $f_3(\lambda)$ and the dotted curve is its normalized wavelength-calibrated spectrum $f_4(\lambda)$ at $z = 45^\circ$. In the bottom frame, the dotted curve is the absorbing component and the dot-dashed curve is the scattering component of $\chi_e(\lambda)$ (solid curve) at $z = 45^\circ$.

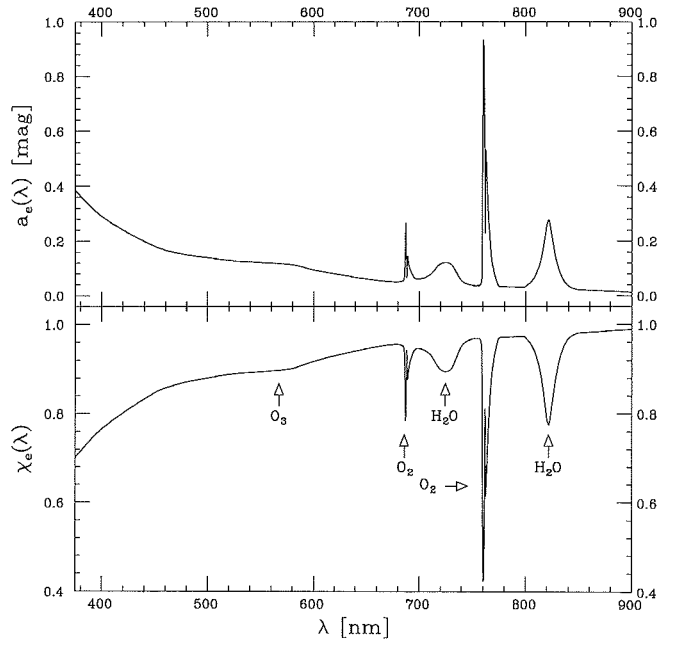


Figure 3: The effects of Aerosol scattering, Rayleigh scattering and the atmospheric molecular absorption of H_2O , O_2 and O_3 upon stellar spectra at $z = 0^\circ$ at ESO. Top curve: $a_e(\lambda)$; bottom curve: $\chi_e(\lambda)$.

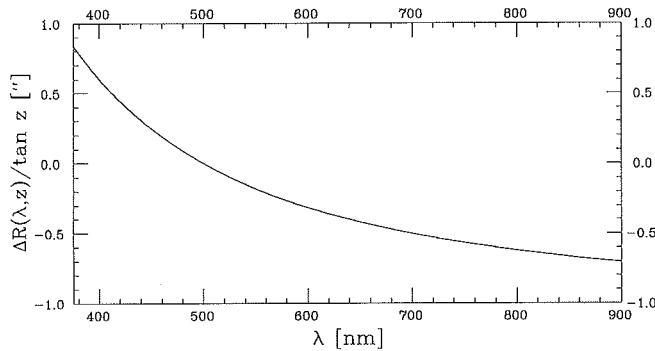


Figure 4: The differential atmospheric refraction.

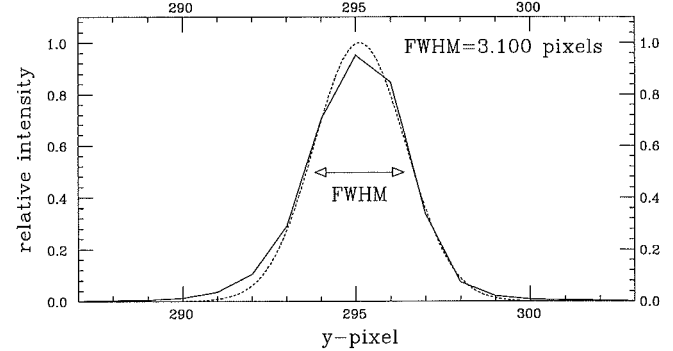


Figure 5: The cross-section of a CCD image and its Gaussian approximation (dotted curve), produced by the MIDAS routine CENTER/GAUSS. FWHM is the full width at half maximum of the Gaussian.

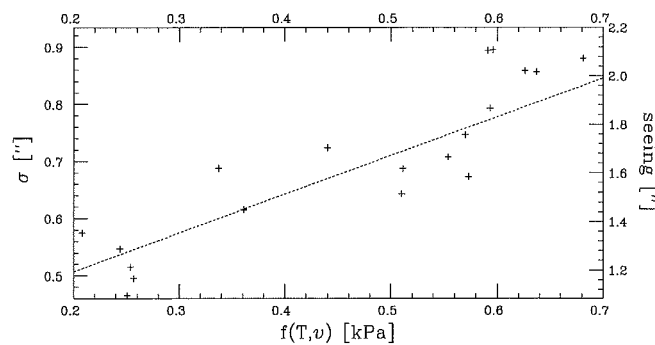


Figure 6: The correlation between the dispersion (seeing) and the vapour pressure.

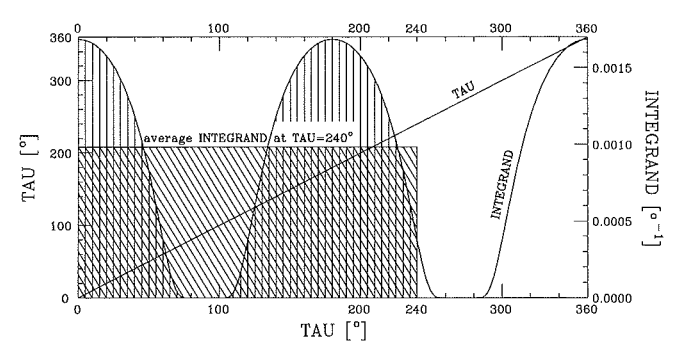


Figure 7: Solving $S_B, c, \sigma(\tau) = \frac{1}{2\pi} \int_0^\tau \exp\left(\frac{-C^2}{2\sigma^2(B^2+1)\cos^2\tau}\right) d\tau$ with MIDAS at $\frac{C^2}{2\sigma^2(B^2+1)} = 0.5$ and $\tau = 240^\circ$.

Table 2: The differential atmospheric mean refraction relative to 500 nm at ESO.

λ [nm]	$\frac{\Delta R(\lambda, z)}{\tan z}$	λ [nm]	$\frac{\Delta R(\lambda, z)}{\tan z}$
375	0'84	650	-0'42
400	0'60	700	-0'50
450	0'25	750	-0'57
500	0'00	800	-0'62
550	-0'18	850	-0'67
600	-0'32	900	-0'70

dimensions and the extended stellar image cannot be simultaneously placed at the same position within the slit at all wavelengths (the star is assumed to be centred at 500 nm). The spectral transmittance function at the spectrograph slit $\chi_s(\lambda)$ is the fraction of stellar light that passes through the slit; the slit length $2b$ depends upon the telescope and the slit widths are chosen by the observer.

3.1 Atmospheric optics

There are two atmospheric quantities to be solved: $\Delta R(\lambda, z)$, the differential atmospheric mean refraction relative to 500 nm and σ , the nocturnal dispersion (seeing) of the (Gaussian) surface brightness of the stellar image. We derived both quantities in the A&A paper from meteorological measurements at ESO; in the present paper we just present the results.

Due to the differential atmospheric refraction, a weakened spectrum enters the telescope and therefore, light of different λ experiences the spectrograph slit differently. The function $\frac{\Delta R(\lambda, z)}{\tan z}$ is plotted in Figure 4 and listed in Table 2.

Small-scale rapidly variable atmospheric turbulences cause a blowing up of stellar images. Our elaborations (Fluks and Thé, 1992) showed that σ is

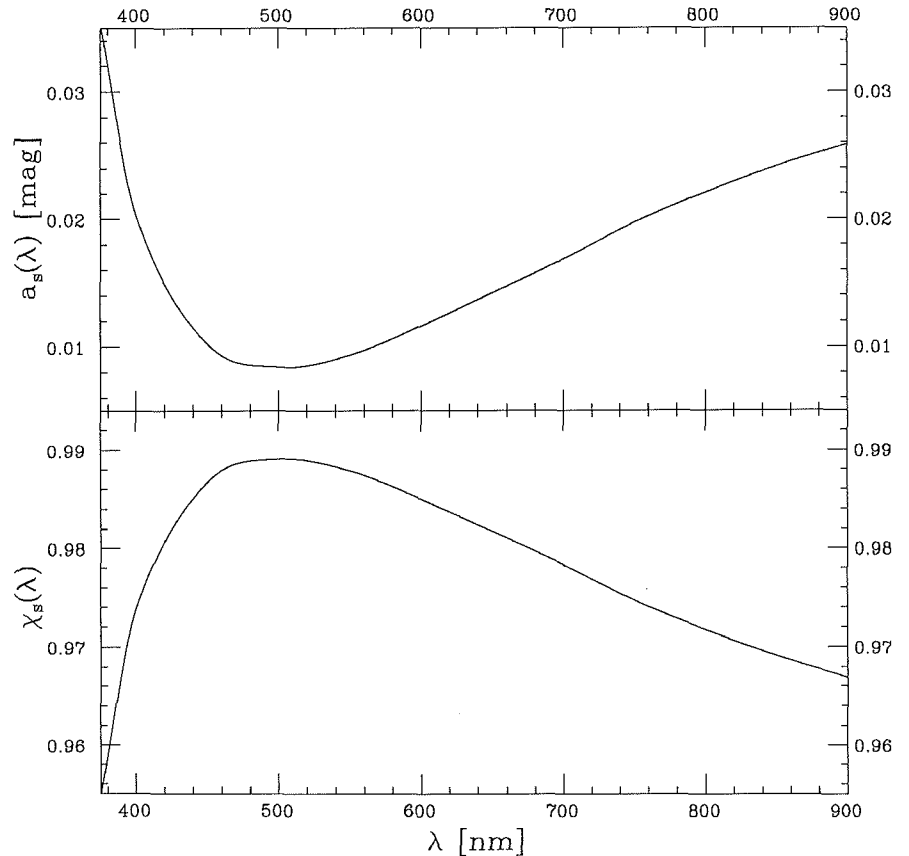


Figure 8: The total effects of differential atmospheric refraction, finite spectrograph-slit dimensions and slit orientation upon a stellar spectrum for a star $z = A = 45^\circ$ with $\sigma = 0'800$ and a horizontal mounted spectrograph-slit of sizes $2a \times 2b = 5'' \times 240''$. Top curve: $a_s(\lambda)$; bottom curve: $\chi_s(\lambda)$.

independent of λ and depends mainly upon the vapour pressure $f(T, \nu)$, a function of the temperature T and the relative humidity ν . This is shown in Figure 6; the datapoints on which the relation between $f(T, \nu)$ and σ is based, are also displayed. There is a link between this relation and the generalization of Brunt's formula (Kondratyev, 1969): in moist and/or warm turbulent air (high vapour pressure) the absorptivity and

thus the re-emissivity of water vapour will be higher and therefore σ broader. The σ s were obtained from the observed CCD intensity-profiles, like the one of Figure 5, and depends on the full width at half maximum (FWHM) and the spatial scale of the telescope.

3.2 The surface brightness

There are two ways to describe the transmittance problem. One can apply the fixed coordinates x and y or the wavelength-dependent coordinates u and v . In the $\{x, y\}$ -system in the plane of the slit, the slit is a fixed rectangle and the surface brightness is ellipsoidal. In the $\{u, v\}$ -system in the elevated plane, the light experiences the slit as an off-centred parallelogram, the surface brightness is circular, and a numerical solution of $\chi_s(\lambda)$ can be found.

3.3 The solution

The key-equation for solving $\chi_s(\lambda)$ is,

$$\chi_s(\lambda) = 1 + \sum_{i=1}^4 (S_{B, c, \sigma}(\tau_i) - S_{B, c, \sigma}(\tau_{i+1})) \leq 1$$

Table 3: MIDAS routines to obtain $S_{B, c, \sigma}(\tau) = \frac{1}{2\pi} \int_0^\tau \exp\left(\frac{-C^2}{2\sigma^2(B^2 + 1)\cos^2 \tau}\right) d\tau$.

STEP	ROUTINE
Midas 001>	Create variable TAU, $0^\circ \leq TAU \leq 360^\circ$ (to be executed just once):
Midas 002>	CREATE/IMAGE TAU 1,10001 0,0.036
Midas 003>	COPY/IT TAU TAU
Midas 004>	COMPUTE/TABLE TAU :TAU = 0.036* (SEQ-1)
Midas 004>	CONVERT/TABLE TAU =TAU :TAU :TAU TAU SPLINE
Midas 005>	Compute INTEGRAND:
Midas 006>	COMPUTE/IMAGE INTEGRAND = COS(TAU)*COS(TAU)/+
Midas 006>	COMPUTE/IMAGE INTEGRAND = EXP (-1/INTEGRAND)/360
Midas 007>	Compute INTEGRAL:
Midas 008>	AVERAGE/COLUMN INTEGRAL = INTEGRAND 0, +
Midas 008>	COMPUTE/IMAGE INTEGRAL = INTEGRAL*#
Midas 009>	FIND/MINIMAX INTEGRAL
	+ : include value for $\frac{C^2}{2\sigma^2(B^2 + 1)}$; #: include value for τ , error $\leq 5 \cdot 10^{-5}$

in which B, C and τ are amalgamations of astrometric, spectrographic, meteorological and optical variables and parameters. The index i refers to a particular part of the slit, determined by lines connecting the slit centre to the vertices. In the A&A paper, the solutions to B, C and τ are given.

In order to obtain $\chi_s(\lambda)$ one has to solve $S_{B,C,\sigma}(\tau)$,

$$S_{B,C,\sigma}(\tau) = \frac{1}{2\pi} \int_0^\tau \exp\left(\frac{-C^2}{2\sigma^2(B^2+1)\cos^2\tau}\right) d\tau$$

A serious complication in the numerical evaluation to $S_{B,C,\sigma}(\tau)$ is that the wavelength appears in τ .

Table 3 shows how MIDAS (release 90NOV) deals with such problems. First, the file TAU is created in 10,000 steps of $0^\circ.036$ each (10001 pixels), starting at $0^\circ:0^\circ \leq \text{TAU} \leq 360^\circ$. MIDAS treats the contents of a file (in this case the contents of the file TAU) as the input in

its computations. As a consequence the file TAU itself, with its pixel values identical to the corresponding world-coordinates, can be considered as a variable. The result is shown in Figure 7 (referring to the left axis of this figure). In the second stage, MIDAS computes

$$\frac{1}{360} \exp\left(\frac{-C^2}{2\sigma^2(B^2+1)\cos^2\tau}\right),$$

named INTEGRAND. The result at

$$\frac{-C^2}{2\sigma^2(B^2+1)}$$

= 0.5 is also displayed in Figure 7 (referring to the right axis of this figure). In the third stage of Table 3 (the integration of INTEGRAND from 0° to 240°) MIDAS computes $S_{B,C,\sigma}(240^\circ)$, named INTEGRAL, as the average of INTEGRAND in the interval $0^\circ \leq \text{TAU} \leq 240^\circ$, multiplied by the interval itself (thus the two hatched areas of Figure 7 cover identical surfaces). Note that $S_{B,C,\sigma}(\tau)$ uses radians whereas MIDAS computes in degrees.

Once the $\chi_s(\lambda)$ s have been solved for the λ s of Table 2, MIDAS produces $\chi_s(\lambda)$ for all λ s by the interpolation-routine CONVERT/TABLE (see also Table 3). The results obtained using the above outlined procedure are displayed in Figure 8. From $\chi_s(\lambda)$, $a_s(\lambda)$ can then be obtained.

References

- Cramer, N. June 1990, *The Messenger*, **60**, 62.
 Filippenko, A. 1982, *PASP*, **94**, 715.
 Fluks, M.A., and Thé, P.S. 1992, *A&A*, **255**, 477.
 Kondratyev, K.YA. 1969, "Radiation in the atmosphere", International geophysics series, volume 12, Academic Press, Chapters 3 to 5.
 Tüg, H. December 1977, *The Messenger*, **11**, 7.
 Valley, S.L. (Ed.) 1965, "Handbook of geophysics and space environments", McGraw-Hill Book Company Inc., Chapters 7, 10 and 16.

A Coronagraph for COME-ON, the Adaptive Optics VLT Prototype

F. MALBET, Observatoire de Paris and Observatoire de Grenoble, France

Thanks to new adaptive optics systems, imaging resolution has reached the diffraction limit of large telescopes in the near-infrared. Numerous aspects of astronomy (spectroscopy, polarimetry,...) will benefit from this progress. Coronagraphic imaging belongs to this category. A coronagraph installed in an adaptive optics system will significantly increase the imaging contrast. In addition, adaptive optics yields stable images and this gives a high efficiency to the coronagraphic imaging. Up to now, an increase in spatial resolution meant a loss in coronagraphic efficiency, for the central star could almost never be exactly aligned with the occulting mask because of the seeing motion. For instance, the smallest mask used to observe the β Pictoris circumstellar disk had a diameter of 4.5 arcsec on the sky, corresponding to 30 AU. However, most of the essential and needed information lies inside this distance.

The coronagraph fitting the COME-ON adaptive optics system has been developed in 1990 in the Département de Recherche Spatiale, at the Observatoire de Paris (Meudon). It was originally designed to detect circumstellar environments around young stellar objects. The optical layout is simple; the

coronagraph elements are inserted between the On-Off mirror and the infrared detector (see Fig. 1). The first lens L1 images the focal plane onto the mask M; the lens L2 then collimates the light onto the Lyot stop, which can be present or not; finally, the lens L3 reimages the focal plane onto the detector with the same aperture ratio as without the coronagraphic system. The optics is made of fluoride glass, to be transparent in the thermal bands. Masks of different size are aligned on a sliding thin plate in order to move quickly from one to another by translation. The masks and the Lyot stop are manufactured by a microphotolithography process. The Lyot stop is only used when the mask size is large compared with the FWHM of the point-spread function FWHM. The masks are movable in X and Y directions by a remote-control motorization. The centring accuracy is about one tenth of the pixel size on the sky. The size of the masks ranges from 95 to 460 microns, which corresponds respectively to 0.27 and 1.3 arcsec on the sky for F/20 aperture. Every element, except the lens L1, is fixed on a movable bench in order for commutation between the normal mode and the coronagraphic one to be fast and easy.

The first test was made in January 1991 at the 3.6-m ESO telescope at La Silla, Chile, during the adaptive optics runs. The vertical motion of the masks was not yet motorized and the centring via the On-Off mirror tilt was accurate to only half a pixel. Therefore, no reliable observations were obtained, but the concept was validated. The second test took place during the April-May 1991 COME-ON run. Although a parasitic reflection in the cryostat strongly limited the elementary integration time for faint stars, we succeeded in obtaining very good coronagraphic images of bright point-like stars (see Fig. 2), in particular Sirius. We did not find the suspected third companion, because the detector field was too small (3 arcsec) and we could only observe during a short period at the beginning of the night.

The main result is the confirmation of the contrast gain. In the case of diffraction-limited coronagraphic imaging, a mask which occults the Airy pattern up to the first dark ring stops 84% of the light. If it stops the light up to the second dark ring, 91% is obscured. It means that the rejection rate (total light to not occulted light ratio) of such a mask is 6.3 in the first case and 11.1 in the second one. With Sirius observed in the